

Amorphous carbon contamination monitoring and process optimization for single-walled carbon nanotube integration

A Jungen, C Stampfer, L Durrer, T Helbling and C Hierold

Micro and Nanosystems, ETH Zurich, 8092 Zurich, Switzerland

E-mail: alain.jungen@micro.mavt.ethz.ch

Received 18 October 2006, in final form 4 December 2006

Published 12 January 2007

Online at stacks.iop.org/Nano/18/075603

Abstract

We detail the monitoring of amorphous carbon deposition during thermal chemical vapour deposition of carbon nanotubes and propose a contamination-less process to integrate high-quality single-walled carbon nanotubes into micro-electromechanical systems. The amorphous content is evaluated by confocal micro-Raman spectroscopy and by scanning/transmission electron microscopy. We show how properly chosen process parameters can lead to successful integration of single-walled nanotubes, enabling nano-electromechanical system synthesis.

1. Introduction

The physics of single-walled carbon nanotubes (SWNTs) has evolved into an ever-growing research field [1]. Their unique structural, mechanical and electrical properties make them ideal for numerous applications [2–5]. Since their discovery, technological advances towards the controlled synthesis of nanotubes [6–8] and, foremost, their integration with systems have been addressed [9–11].

Catalytic thermal chemical vapour deposition (CVD) processes to synthesize SWNTs from methane with high structural perfection were enabled by Kong and co-workers [12]. High temperatures were reported to be necessary to form SWNTs with small diameters and which were nearly defect-free. Plasma-enhanced CVD has been reported to significantly reduce the growth temperature; however, the sample biasing due to the plasma potential preferentially results in vertically grown nanotubes with considerable defects which are not suitable for integrated and interconnected SWNT-based systems [13]. The catalytic thermal CVD process is accompanied by a self-decomposition of methane, resulting in non-catalytic amorphous carbon (a-C) deposition. Depending on the level of integration and on the application, this unwanted a-C coating can lead to device failure. In nanoelectronics, for instance, the electrical properties of the SWNTs can suffer from leakage currents. In nanomechanics, SWNTs need to be released from the supporting SiO₂ surface; however, a thick a-C over-coating can prevent SiO₂ from being dissolved.

In this paper, we address the issue of a-C deposition during various thermal CVD processes. The amount and the structural components of the a-C film were measured by confocal Raman scattering together with electrical measurements and release attempts. We also demonstrate a recipe for producing releasable SWNTs with high structural quality and reduced a-C.

2. Experimental setup

The reaction furnace was an ATV PEO 603 LPCVD system which can be operated at a base pressure of about 10⁻⁵ mbar. The reaction chamber consists of an externally heated quartz glass (hot wall) holding wafers up to 6 inches in diameter. The temperature is monitored at three different locations inside the chamber and uniform temperature is maintained by three individual controllers. The gas residence time is identical to the process time, which was 15 min, and the pressure regime was purely static (no gas flow during process). Room-temperature Raman spectra were recorded from a WITec CRM200 confocal micro-Raman spectroscope using a 532 nm green laser delivered through a single mode optical fibre. This type of fibre supports only a single transversal mode which can be focused to a diffraction-limited spot of about 400 nm (100× objective of NA = 0.8). The backscattered light was cut by a super-notch filter and focused into a 50 μm pinhole. The spectrometer was equipped with a Peltier-cooled charge coupled device (CCD) camera. The spectral resolution was 1 cm⁻¹. Precise positioning of the sample under the laser

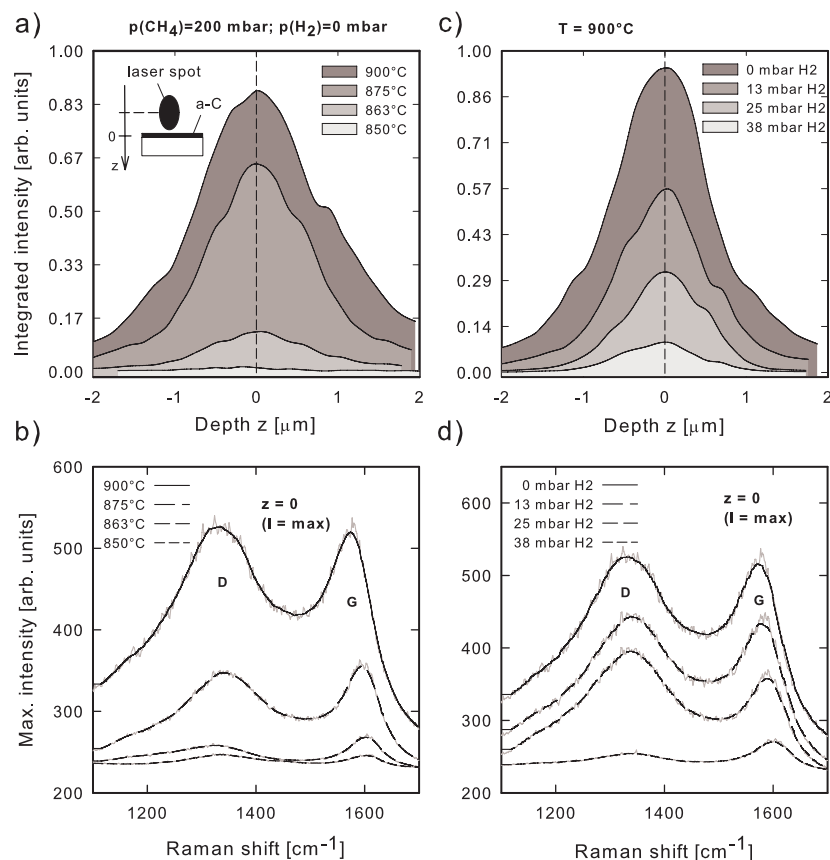


Figure 1. (a) Integrated D- and G-band Raman spectra for various process temperatures. (b) Maximum Raman intensity spectra of the D- and G-band for various process temperatures. Methane pressure: 200 mbar, no hydrogen. (c) Integrated D- and G-band Raman spectra by depth scan for various H₂ (and CH₄) pressures. (d) Maximum Raman intensity spectra of the D- and G-band for various partial pressures of H₂. The methane partial pressure varied accordingly as $p(\text{CH}_4) = 200 - p(\text{H}_2)$ mbar. Process temperature: 900 °C.

spot was monitored with piezoelectric actuators with a travel range of $200 \times 200 \times 20 \mu\text{m}^3$ in the x , y and z directions respectively. The Raman system was calibrated as described elsewhere [14]. Optical inspection was performed using a Zeiss Ultra 55 scanning electron microscope (SEM) operated at 5 kV and a Philips CM200 transmission electron microscope (TEM) operated at 120 kV.

For the study of the structure of the carbons, two Raman features were exploited, the so-called D- and G-peaks, which lie around 1350 and 1590 cm^{-1} , respectively. Extensive studies on different graphitic films had been conducted, and readers are referred to [15–18]. For simplicity, we used the same spectral definitions and terminology as in [16]. We emphasize that the deposited carbon layers described in this paper can have various degrees of ordering aside from pure graphite (sp^2) and diamond (sp^3) which are collectively termed ‘amorphous carbon’ (a-C). As a consequence a-C refers here rather to a contaminative carbon deposit than to ‘pure’ a-C.

3. Results and discussions

3.1. Influence of CVD parameters

Amorphous carbon formation can be avoided by preventing the hydrocarbon gas from entering self-pyrolysis. As this self-decomposition does not require a catalytic additive and as the

Raman signal from well-crystallized nanotubes correlates with the signal from a-C, experiments were made on catalyst-less silicon oxide chips. Figure 1(a) shows the summed D- and G-peak Raman intensities I of a-C coated chips from CVD runs at various temperatures. The summation was done as a function of the vertical z -displacement of the laser spot. This allowed for precise focusing of each sample, which is a requirement when comparing the signal intensity between the samples. The focus position $z = z(I_{\text{max}})$ of every sample was stored in the system, and the summed intensity is plotted as a function of the laser displacement relative to $z = 0$. Figure 1(b) shows the Raman spectra of the samples from (a). Here, each spectrum was obtained by averaging 256 spectra from planar x -, y -scans of 4 by $4 \mu\text{m}^2$ over a portion of the a-C layer while z was locked to $z = 0$ to yield the maximum Raman signal. The presence of a-C is indicated by two spectral features at approximately 1350 and 1600 cm^{-1} . The signal intensity $I(\text{D})$, $I(\text{G})$ of both peaks increased with increasing process temperature. This is an indicator of enhanced a-C deposition at higher temperatures.

In the following we considered the methane/hydrogen gas composition ratio to study its influence on the a-C production [19]. Several CVD processes were performed with the partial pressure of hydrogen varying from 0 to 100 mbar at a process temperature of 900 °C. The total

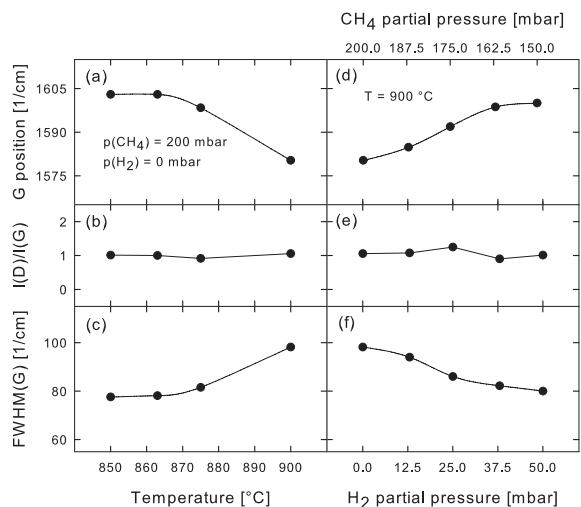


Figure 2. Extracted Raman data obtained directly from the spectra shown in figure 1. (a) G-peak position, (b) D- to G-peak intensity ratio, (c) full width at half maximum of the G-peak. Tracking of the process run for lower temperatures was impossible as the Raman features could not be observed. (d) G-peak position, (e) D- to G-peak intensity ratio, (f) G-peak FWHM for processes of varying gas mixtures.

pressure (the sum of the partial pressures of H_2 and CH_4) was kept constant at 200 mbar. The Raman measurements shown in figures 1(c), (d) were obtained in the same way as the plots (a), (b). It is seen that the intensity reduces gradually with the addition of hydrogen (and with the reduction of methane). Similarly, the a-C layer thickness increased for reduced hydrogen amount.

Both CVD parameters (temperature and hydrogen amount) were shown to influence the Raman intensity of the deposited a-C greatly. As the Raman intensity is directly proportional to matter abundance one can assume that the intensity is strongly related to the deposited a-C amount or layer thickness. However, visible Raman spectroscopy is reported to be 50–250 times more sensitive to sp^2 (graphite) sites than to sp^3 (diamond) sites, as visible photons preferentially excite their π -states¹ [20–22]. Changes in the Raman intensities seen in figure 1 can thus be due to both structural changes in the carbon bindings and layer thickness changes. The G-position, intensity $I(D)/I(G)$ -ratio and the full width at half maximum FWHM(G) are plotted as a function of temperature and gas mixture in figure 2. Looking at the G-peak position shown in (a) and (d), a downshift can be observed with increasing temperature and decreasing hydrogen amount in the gas mixture. No trend can be seen in the development of the $I(D)/I(G)$ -ratio which remains at approximately 1. The FWHM(G) shows an increasing trend for increased process temperature and reduced hydrogen content.

From these plots we expect some minor structural changes in the carbonaceous layer. The G-position of nanocrystalline graphite is reported to be at 1600 cm^{-1} , whereas the same peak of pure a-C drops to 1510 cm^{-1} . Figure 2(a) shows a peak softening from 1597 to 1582 cm^{-1} with increasing temperature

¹ Only high-energy Raman spectroscopy from UV sources can reach the σ -states from all types of carbon bindings. Our excitation energy of 2.33 eV is thus only probing the sp^2 content.

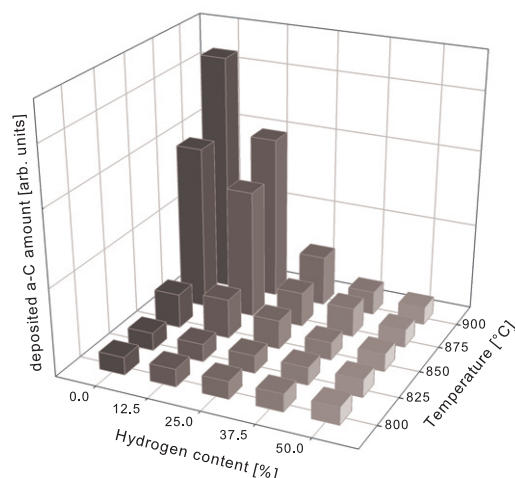


Figure 3. Monitored a-C deposit for various gas mixtures and temperature combinations by Raman scattering.

and reduced hydrogen amount. Thus, the deposited carbon layer shows some alternating degree of ordering. The introduction of defects caused the G-phonon mode to soften to 1582 cm^{-1} , which corresponds to an amorphization towards a-C. This observation is substantiated by the increase of the FWHM(G) seen in figure 2(c), which is an indicator for increasing structural disorder. However, the structural changes are small compared to the amorphization towards pure a-C as the ratio between the D- and G-peak intensities showed no trend. By matching the G-positions and $I(D)/I(G)$ ratios with studies from [18] we found the hydrogen content to be weak ($<8\text{ at.}\%$). Precise hydrogen content measurement can be extracted from multi-wavelength Raman spectroscopy or electron energy-loss spectroscopy [23–25]. To conclude the study of the CVD parameters dependence, we found thicker a-C layers for increasing process temperatures and reduced addition of hydrogen in the reaction gas. At the same time, the carbon bindings showed a weak disordering with increasing temperature and reduced hydrogen amount. Given the weak structural changes, we assume the changes in the Raman intensity to be mainly due to the changes in the deposited layer thickness.

The graph in figure 3 shows the amount of deposited a-C by means of the measured maximum G-peak intensity for 5×5 process combinations between 0 and 50% hydrogen content and a temperature range between 800 and $900\text{ }^\circ\text{C}$. The plot reflects the importance of the addition of hydrogen to the methane mixture to reduce the a-C amount. Independently, reducing the process temperature also contributed to reducing the amount of carbon deposit.

3.2. a-C layer leakage currents and releasability

The presence of a-C on top of a device can exhibit leakage currents. For each sample the resistance on the oxide along a path of $\sim 10\text{ }\mu\text{m}$ was measured. In the absence of an a-C layer a very high resistance, of the order of several hundred $\text{M}\Omega$, was measured. The samples with a detectable a-C layer display a considerably lower resistance, depending on the amount of a-C deposited. The results are shown in table 1. We point out the fact that the (small) structural changes in the carbon bonds

Table 1. LPCVD runs from varying temperature T ($^{\circ}\text{C}$) and hydrogen amount $p(\text{H}_2)$ (mbar) with [$p(\text{CH}_4) + p(\text{H}_2) = 200$ mbar], listing the G-peak intensity $I(\text{G})$ [CCD counts], the electrical resistance R ($\text{k}\Omega$) of the a-C film and HF-test. 'Releasable?' describes the success of the acidic HF etch of the silicon oxide.

T	$p(\text{H}_2)$	$I(\text{G})$	Resistance	Releasable?
800	0	230 ± 4	∞	Yes
850	0	240 ± 2	∞	Yes
863	0	270 ± 2	131 ± 11.5	Yes
875	0	360 ± 2	4.92 ± 0.53	No
900	0	530 ± 2	1.98 ± 0.12	No
900	13	488 ± 2	1.78 ± 0.10	No
900	25	390 ± 2	2.52 ± 0.17	No
900	38	272 ± 2	∞	Yes
900	50	239 ± 2	∞	Yes
900	100	230 ± 4	∞	Yes

might have contributed to the measured conductance changes. However, their influence is low compared to the strong material thickness changes which provided observable changes in chip opacity.

After the resistance measurement, attempts were made to etch the SiO_2 by immersing the chips in concentrated HF (40%) for 5 min. Structures with very little or zero leakage current were found to be releasable, whereas thick a-C layers (with resistances below 100 $\text{k}\Omega$) prevented the latter. These results are summarized in table 1. They show a correlation

between the Raman intensity of the G-peak and the electrical resistance through the same carbon layer. Layers which yielded a resistance in the $\text{k}\Omega$ range prevented the HF acid from dissolving the underlying SiO_2 . From figure 3 and table 1 one can thus define regions of either *reduced* or *high* a-C amount/contamination.

3.3. SWNT growth with reduced a-C

SWNTs typically have small diameters of about 1 nm and thus require small catalyst particles and high growth temperatures [26, 27]. Note that at such high temperatures acetylene is not stable and methane must be used. Delzeit *et al* reported SWNT growth using a 10 nm Al support layer below a 1 nm metal catalyst like Fe, under a growth temperature of 900°C and under pure methane [28]. The results from figure 3 show that using pure methane at 900°C with our specific LPCVD system is not allowed for contamination-free SWNT integration. Increasing the hydrogen in the gas mixture, next to reducing the a-C amount, decreases the rate of CH_4 decomposition by hydrogenating the reactive carbon species (the carbon feedstock) [29, 30]. This, together with the fact that fewer CH_4 molecules are present in the mixture, results in a strongly reduced SWNT density. At a pressure ratio of 50% hydrogen only a few SWNTs were observed which lowered the system yield of SWNT-based nano-electromechanical system (NEMS) devices. Optimal tube density was found for a partial pressure ratio of 150 mbar $\text{CH}_4/50$ mbar H_2 .

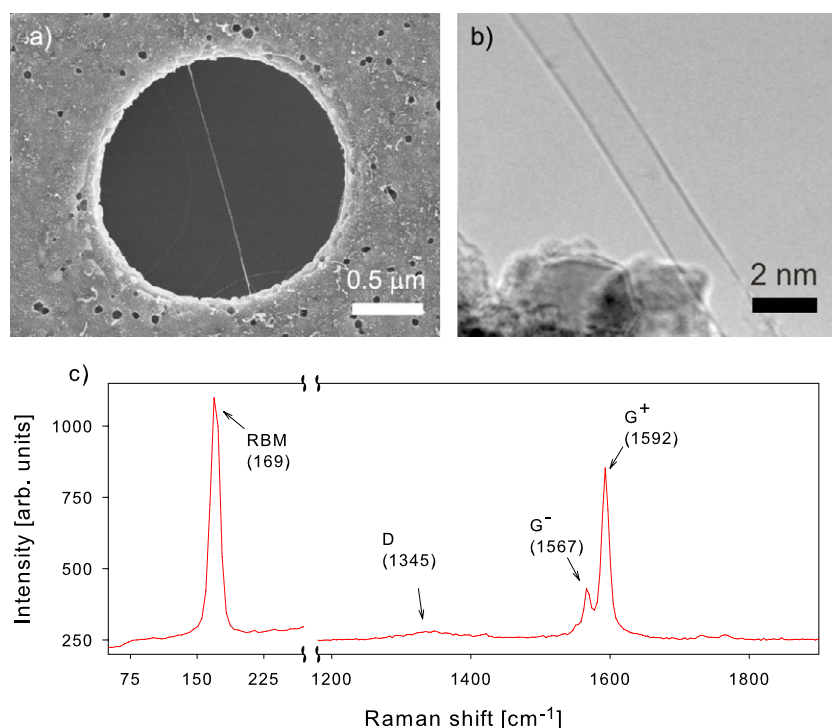


Figure 4. (a) Example of a MEMS device with incorporated carbon nanotubes grown at 850°C from a 10 nm Al/1 nm Ni bi-layer under 150 mbar $\text{CH}_4/50$ mbar H_2 for 15 min. (b) TEM image from SWNT from the same MEMS chip. The sample preparation is detailed in [31]. (c) Raman spectrum recorded from an integrated SWNT synthesized from the aforementioned process. An RBM feature and split G-band features together indicate the presence of SWNT. The weak D-band signal around 1350 cm^{-1} indicates little tube defects (integration time: 20 s).

(This figure is in colour only in the electronic version)

Based on the presented process results, SWNTs were integrated into microsystems and analysed. Micro-electro-mechanical systems (MEMS) were fabricated using a surface micromachining process detailed in [32]. They incorporate up to three structural layers of polycrystalline silicon sandwiching silicon oxides of various thicknesses. Catalyst was deposited onto the topmost layer by sputtering a 10 nm Al/1 nm Ni bi-metal. Chips were then heated under Ar to a temperature of 850 °C. Hydrogen pretreatment was performed for 10 min at a pressure of 200 mbar. Then, thermal CVD under a 150 mbar/50 mbar mixture of CH₄/H₂ at 850 °C during 15 min was carried out for the growth of SWNTs. Cooling was done in vacuum and nitrogen venting after cooling to at least 250 °C. After growth, the chip was subjected to an acidic wet-etch. The success of the release is demonstrated in figure 4(b) as the MEMS layer detached from its supporting substrate and became available for TEM. The technique to perform TEM from SWNT-embedded MEMS is detailed in [31]. The TEM image in figure 4(b) shows a regular, straight SWNT with few defects and a-C. Figure 4(c) shows the Raman spectrum from an integrated SWNT into a MEMS obtained with the aforementioned process. The spectrum shows a typical G feature splitting and a single radial breathing mode (RBM) specific for individual SWNTs [33]. The weak defect-induced D-peak indicates an SWNT with little defects. We note that the $I(D)/I(G)$ ratio cannot be compared to the spectra shown previously in figure 1 as the latter did not incorporate SWNTs but solely a-C. In the present Raman spectrum, the G-peak is dominated by the high-energy mode of the SWNT while the D-peak is a sum of a-C around the tube diameter and the defects in the tube.

4. Conclusions

We have described a method of monitoring the a-C deposition during the CVD growth of high-quality SWNTs directly into MEMS. The amount and the structural components of the a-C film were measured by Raman scattering. Leakage current measurements and HF-release attempts were conducted to sense the impact of a-C presence on the fabrication of MEMS with SWNTs. Both the temperature and the gas composition are found to strongly affect the amorphous carbon deposition. While a high partial pressure of CH₄ provides a rich feedstock for SWNT growth, it also increases the possibility of carbon recombination to a-C. A recipe was provided which complies with the requirements of high-quality nanotubes embedded as a functional NEMS device.

Acknowledgments

This research was supported by ETH FIRST clean room and EMEZ electron microscopy shared facilities. The authors would like to thank R Grunbacher, A C Ferrari, B Babic and M Height for helpful discussions. We would like specifically to thank C Casiraghi and S Stoll for supporting the spectrum fitting and J C Meyer for TEM images. AJ acknowledges funding support from the Swiss National Science Foundation (Grant No. 200021-108059/1) and CS acknowledges support from ETH Zurich (Grant No. TH-18/03-1).

References

- [1] Reich S, Thomsen C and Maultsch J 2004 *Carbon Nanotubes: Basic Concepts and Physical Properties* (Weinheim: Wiley-VCH Verlag GmbH)
- [2] Bachtold A, de Jonge M, Grove-Rasmussen K and McEuen P L 2001 *Phys. Rev. Lett.* **87** 166801
- [3] Schoenenberger C, Bachtold A, Strunk C, Salvétat J P and Forro L 1999 *Appl. Phys. A* **69** 283
- [4] Frank S, Poncharal P, Wang Z L and de Heer W A 1998 *Science* **280** 1744
- [5] Wildoer J W G, Venema L C, Rinzler A G, Smalley R E and Dekker C 1998 *Nature* **391** 59
- [6] Hofmann S *et al* 2005 Catalyst patterning methods for surface-bound chemical vapor deposition of carbon nanotubes *Appl. Phys. A* **81** 1559–67
- [7] Jungen A, Stampfer C, Hoetzel J, Bright V M and Hierold C 2006 Process integration of carbon nanotubes into microelectromechanical systems *Sensors Actuators A* **130–131** 588–94
- [8] Hata K, Futaba D N, Mizuno K, Namai T, Yumura M and Iijima S 2004 Water-assisted highly efficient synthesis of impurity-free single-walled carbon nanotubes *Science* **306** 1362–4
- [9] Baughman R H, Zakhidov A A and de Heer W A 2002 Carbon nanotubes—the route toward applications *Science* **297** 787–92
- [10] Duesberg G S, Graham A P, Liebau M, Seidel R, Unger E, Kreupl F and Hoenlein W 2003 Growth of isolated carbon nanotubes with lithographically defined diameter and location *Nano Lett.* **3** 257–9
- [11] Seidel R V, Graham A P, Kretz J, Rajasekharan B, Duesberg G S, Liebau M, Unger E, Kreupl F and Hoenlein W 2005 Sub-20 nm short channel carbon nanotube transistors *Nano Lett.* **5** 147–50
- [12] Kong J, Soh H, Cassell A, Quate C F and Dai H 1998 Synthesis of individual single-walled carbon nanotubes on patterned silicon wafers *Nature* **395** 878–80
- [13] Hofmann S, Ducati C, Robertson J and Kleinsorge B 2003 Low-temperature growth of carbon nanotubes by plasma-enhanced chemical vapour deposition *Appl. Phys. Lett.* **83** 135–7
- [14] Jungen A, Stampfer C and Hierold C 2006 Thermography on a suspended microbridge using confocal Raman scattering *Appl. Phys. Lett.* **88** 191901
- [15] Tuinstra F and Koenig J L 1970 Raman spectrum of graphite *J. Chem. Phys.* **53** 1126
- [16] Ferrari A C and Robertson J 2000 Interpretation of Raman spectra of disordered and amorphous carbon *Phys. Rev. B* **61** 14095–107
- [17] Ferrari A C and Robertson J 2001 Resonant Raman spectroscopy of disordered, amorphous, and diamondlike carbon *Phys. Rev. B* **64** 075414
- [18] Casiraghi C, Ferrari A C and Robertson J 2005 Raman spectroscopy of hydrogenated amorphous carbon *Phys. Rev. B* **72** 085401
- [19] Li Y M, Kim W, Zhang Y G, Rolandi M, Wang D W and Dai H 2001 Growth of single-walled carbon nanotubes from discrete catalytic nanoparticles of various sizes *J. Phys. Chem. B* **105** 11424–31
- [20] Sails S R, Gardiner D J, Bowden M, Savage J and Rodway D 1996 Monitoring the quality of diamond films using Raman spectra excited at 514.5 nm and 633 nm *Diamond Relat. Mater.* **5** 589–91
- [21] Anastassakis E and Burstein E 1970 Electric-field-induced infrared absorption and Raman scattering in diamond *Phys. Rev. B* **2** 1952–65
- [22] Loudon R 1964 The Raman effect in crystals *Adv. Phys.* **13** 423–82
- [23] Wehenkel C and Gauthe B 1974 Electron energy loss spectra and optical constants for the first transition series from 2 to 120 eV *Phys. Status Solidi b* **64** 515–25

- [24] Kimura T, Muto S, Tatsumi K, Tanabe T and Kiyobayashi T 2006 Intercalated hydrogen in nanostructured graphite studied by electron energy-loss spectroscopy and molecular orbital calculations *J. Alloys Compounds* **413** 150–4
- [25] Adamopoulos G, Robertson J, Morrison N A and Godet C 2004 Hydrogen content estimation of hydrogenated amorphous carbon by visible Raman spectroscopy *J. Appl. Phys.* **96** 6348–52
- [26] Graham A P, Duesberg G S, Seidel R, Liebau M, Unger E, Kreupl F and Hoenlein W 2004 Towards the integration of carbon nanotubes in microelectronics *Diamond Relat. Mater.* **13** 1296–300
- [27] Paillet M, Jourdain V, Poncharal P, Sauvajol J-L, Zahab A, Meyer J C, Roth S, Cordente N, Amiens C and Chaudret B 2004 Versatile synthesis of individual single-walled carbon nanotubes from nickel nanoparticles for the study of their physical properties *J. Phys. Chem.* **108** 17112–8
- [28] Delzeit L, Chen B, Cassell A, Stevens R, Nguyen C and Meyyappan M 2001 Multilayered metal catalysts for controlling the density of single-walled carbon nanotube growth *Chem. Phys. Lett.* **348** 368–74
- [29] Franklin N R, Li Y, Chen R J, Javey A and Dai H 2001 Patterned growth of single-walled carbon nanotubes on full 4-inch wafers *Appl. Phys. Lett.* **79** 4571–3
- [30] Dean A M 1990 Detailed kinetic modeling of autocatalysis in methane pyrolysis *J. Phys. Chem.* **94** 1432–9
- [31] Jungen A, Stampfer C, Durrer L, Helbling T and Hierold C 2006 A method for enhanced analysis of specific as-grown carbon nanotubes *Phys. Status Solidi b* **243** 3138–41
- [32] Bustillo J M, Howe R T and Muller R S 1998 Surface micromachining for microelectromechanical systems *Proc. IEEE* **86** 1552–74
- [33] Jorio A, Saito R, Hafner J H, Lieber C M, Hunter M, McClure T, Dresselhaus G and Dresselhaus M S 2001 Structural (n, m) determination of isolated single-wall carbon nanotubes by resonant Raman scattering *Phys. Rev. Lett.* **86** 1118–21